

Gamma-ray orbital modulation of the transitioning millisecond pulsar binary XSS J12270–4859

HONGJUN AN¹

¹*Department of Astronomy and Space Science, Chungbuk National University, Cheongju, 28644, Republic of Korea*

ABSTRACT

We report on gamma-ray orbital modulation of the transitioning millisecond pulsar binary XSS J12270–4859 detected in the *Fermi* Large Area Telescope (LAT) data. We use long-term optical data taken with the *XMM-Newton* Optical Monitor and the *Swift* UltraViolet Optical Telescope to inspect radio timing solutions that are limited to relatively short time intervals, and find that extrapolation of the solutions aligns well the phasing of the optical data over 15 years. The *Fermi*-LAT data folded on the timing solutions exhibit significant modulation ($p = 5 \times 10^{-6}$) with a gamma-ray minimum at the inferior conjunction of the pulsar. Intriguingly, the source seems to show similar modulation in both the low-mass X-ray binary (LMXB) and the millisecond pulsar (MSP) states, implying that mechanisms for gamma-ray emission in the two states are similar. We discuss these findings and their implications using an intra-binary shock scenario.

1. INTRODUCTION

Spider pulsar binaries (pulsar binaries hereafter) are composed of a millisecond pulsar (MSP) and a low-mass companion, where the companion surface is heated and evaporated by the pulsar’s irradiation. In a pulsar evolutionary scenario (e.g., [Bhattacharya & van den Heuvel 1991](#)), pulsar-binary systems are believed to be descendants of low-mass X-ray binaries (LMXBs) in which the low-mass companion loses its mass and the neutron star spins up by accretion over a long time (\sim Gyr; [Alpar et al. 1982](#); [Bhattacharya & van den Heuvel 1991](#)). When the accretion is quenched, the systems are observed as pulsar binaries. This evolutionary scenario is supported by discoveries of objects that have exhibited transitions between an accretion-powered LMXB and a rotation-powered MSP state ([Archibald et al. 2009](#); [Papitto et al. 2013](#); [Bassa et al. 2014](#)).

Emission mechanisms of transitioning systems in the LMXB and the MSP states differ. In the MSP state, like in pulsar binaries, the companion is heated by the pulsar’s energy output and so exhibits day-night cycles. The heating can make the companion wind strong, and it interacts with the pulsar wind to form an intra-binary shock (IBS; e.g., [Wadiasingh et al. 2017](#); [Kandel et al. 2019](#); [van der Merwe et al. 2020](#)). Pulsar wind particles

are accelerated in the shock and emit synchrotron radiation, producing characteristic double peaks in the X-ray light curve around a maximum (e.g., [Roberts et al. 2015](#)). Gamma rays are produced primarily in the pulsar magnetosphere, but inverse-Compton scattering (ICS) of the stellar blackbody radiation by energetic particles in the shock or in the pre-shock pulsar wind can also produce gamma-ray radiation in the GeV band; this ICS emission may exhibit orbital modulation due to variation of the viewing geometry, having a maximum or minimum at the pulsar’s conjunctions (e.g., [An et al. 2020](#); [Clark et al. 2021](#)).

In the LMXB state, the optical and X-ray emissions are mostly powered by accretion. The surface of the pulsar can be heated by channeled accretion and so X-ray pulsations are detected ([Archibald et al. 2015](#); [Papitto et al. 2015](#)). Because the accretion can be unstable, orbital light curves in the optical and X-ray bands exhibit dips and flares (e.g., [de Martino et al. 2013](#); [Tendulkar et al. 2014](#)). The gamma-ray emission mechanism, other than the magnetospheric one, in this state is rather unclear. A model suggests that the IBS is destroyed by the strong accretion and gamma rays are produced by the synchrotron-self-Compton process at the interface between the magnetosphere and accretion disk ([Papitto et al. 2014](#)). Alternatively, it was suggested that ICS of disk photons by the pre-shock pulsar wind is responsible for the gamma rays (e.g., [Takata et al. 2014](#)). In these scenarios, orbital modulation in the gamma-ray band seems unlikely since conditions for the emission do not vary over the orbit.

Corresponding author: Hongjun An
hjan@cbnu.ac.kr

Table 1. Optical data used in this work

Inst.	Filter	Nobs	Obs. ID	Time (MJD)
UVOT	v	18	35101001–82011001	53628–57195
UVOT	u	29	35101003–95612003	56319–59184
OM	U	1	551430401	54837
OM	U	1	656780901	55562
OM	U	1	727961401	56656
OM	U	1	729560801	56835

XSS J12270–4859 (4FGL J1228.0–4853; J1227 hereafter) is a transitioning MSP (tMSP) which transitioned from an LMXB to an MSP state late 2012 (\sim MJD 56250; Bassa et al. 2014). Radio timing studies (Roy et al. 2015; de Martino et al. 2020) revealed that the source has a 1.69 ms pulsar in a 6.9 hr orbit with a G-type companion (de Martino et al. 2015). After the transition, the source was well studied at X-rays, and the characteristic double-peak X-ray light curve was clearly detected with a maximum at the pulsar’s inferior conjunction (de Martino et al. 2020), as expected in IBS scenarios if the stellar wind is stronger than the pulsar’s (e.g., Kandel et al. 2019). In the gamma-ray band, the pulsar’s pulsations were detected over a relatively short time period after the transition (Johnson et al. 2015), and weak orbital modulation ($\leq 3\sigma$) in 1.6 years of > 300 MeV data taken with *Fermi* Large Area Telescope (LAT; Atwood et al. 2009) was suggested (Xing & Wang 2015, ; XW15 hereafter). In that work, the gamma-ray orbital modulation had a ‘maximum’ at the pulsar’s inferior conjunction (IFC; pulsar between the companion and observer). Since *Fermi* LAT has been collecting data for more than 12 years, the orbital modulation may be detected with higher confidence and characterized better.

In this paper, we investigate the gamma-ray modulation in J1227 using 12.5 years of data taken with *Fermi* LAT. Since radio timing solutions that we found in the literature do not cover the whole time period of the LAT data, we inspect the timing solutions using optical data taken with *XMM-Newton* Optical Monitor (OM) and *Swift* UltraViolet Optical Telescope (UVOT). We use the timing solutions that adequately explain the phasing of the long-term optical data for a LAT timing analysis. We present optical data analysis and verify the timing solutions using the phasing of the optical light curves in § 2. We report analysis results of the *Fermi* LAT data in § 3, and discuss in § 4.

2. OPTICAL DATA ANALYSES

Orbital periods of pulsar binaries can vary slightly over time, and radio timing solutions for J1227 obtained over short time intervals (c.f., > 12.5 year of LAT op-

eration) require one or two orbital-period derivatives (Roy et al. 2015; de Martino et al. 2020). They may reflect long-term changes of the orbital motion or a small but unpredictable variation as seen in other pulsar binaries (e.g., $\Delta P_B/P_B \leq 10^{-6}$ for PSR J2039–5617; Clark et al. 2021). In the latter case, the short-term radio timing solutions may be valid only within the given intervals. Hence we check to see if the ‘orbital’ (not the pulsar spin) solutions are valid over the 12.5-yr period. This can be done by carefully phasing the day-night cycles of the companion emission which is expected to be maximum at the binary phase $\phi_B \approx 0.75$ (defined to be IFC). For this test, we use optical photometric data collected with the *XMM-Newton* OM and the *Swift* UVOT over a period of 15 years (MJD 53628–59184).

2.1. Optical Data Reduction

We use *Swift* and *XMM-Newton* data taken between 2005 Sep. and 2020 Dec. There are 63 *Swift* and 4 *XMM-Newton* observations in the period (Table 1). The *Swift* UVOT observations are made with various filters, but we use the v- or u-filter data only since the source is well detected in those bands. The *XMM-Newton* data are all made with the U filter.

For the *Swift* data analysis, we use an $R = 5''$ aperture for the source and an $R = 7.5''$ aperture in a source-free region for the background extraction. We process the data with HEASoFT v6.27 following the standard UVOT analysis procedure¹ to measure the AB magnitude in each frame. The observation times are barycenter-corrected using the barycenter-corrected XRT arrival times in each observation for the source position R.A.=186.99468° and Decl.=−48.89521° (Roy et al. 2015).

We process the *XMM-Newton* OM data with XMM-SAS v20190531.1155 following the standard procedure.² The arrival times are barycenter-corrected with the **barycen** tool of SAS, and the measured count rates are converted into AB magnitudes.³ The light curves are then constructed with 300-s time bins.

Figure 1 shows *Swift* and *XMM-Newton* optical light curves folded on the timing solutions in Table 2. The light curves show well the day-night cycles of the companion emission. The *Swift* data cover various epochs over 15 years; the v- and u- band data were taken mostly in the pre-transition and post-transition state, respec-

¹ <https://www.swift.ac.uk/analysis/uvot/>

² <https://www.cosmos.esa.int/web/xmm-newton/sas-thread-omf>

³ <https://www.cosmos.esa.int/web/xmm-newton/sas-watchout-uvflux>

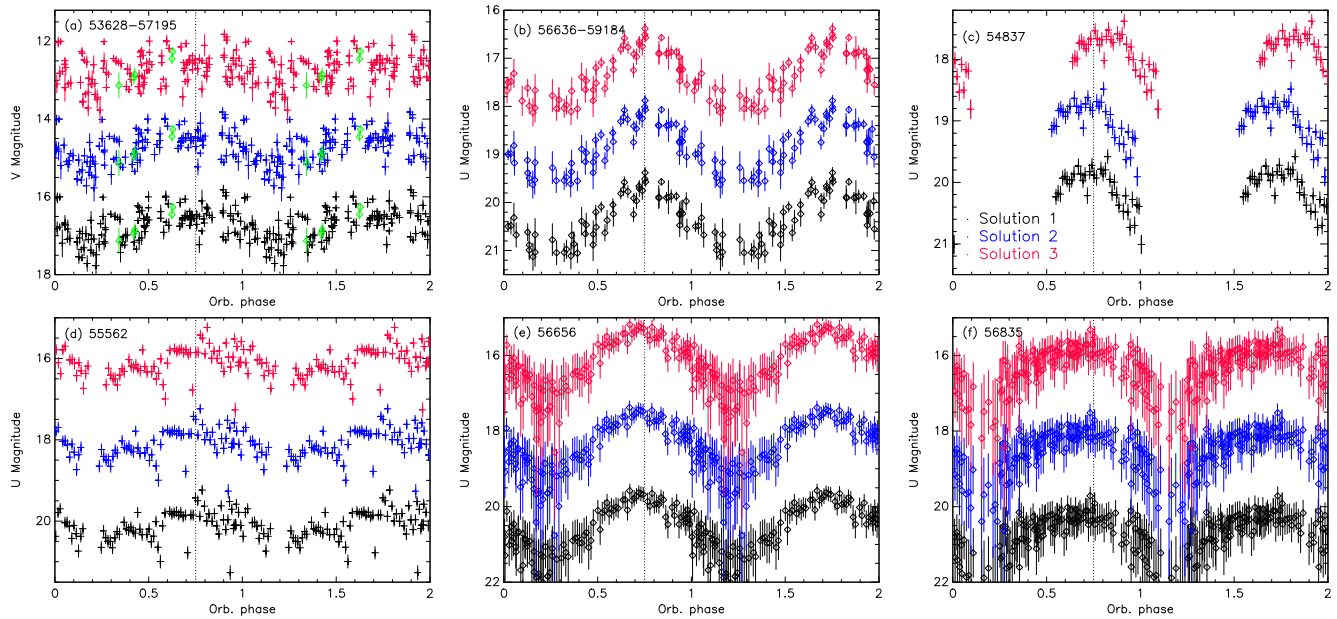


Figure 1. Optical light curves folded on timing solutions found in literature (black, blue, and red for Solutions 1, 2 and 3, respectively; Table 2). The blue and red light curves are displaced vertically, and pre- and post-transition data are plotted in crosses and diamonds, respectively. Phase 0 is the ascending node, and the vertical dotted line denotes the IFC phase. (a): *Swift* v-band data. Most of the v-band data are taken before the transition (<MJD 56250). Five data points plotted in green are taken after the transition, have higher magnitudes than the pre-transition ones, and are vertically displaced. (b): *Swift* u-band data. (c-f): *XMM-Newton* U-band data on MJD 54837 (c), MJD 55562 (d), MJD 56656 (e) and MJD 56835 (f).

tively. Notice that pre-transition (LMXB state) light curves (panels a, c, and d) exhibit some dips and flares.

2.2. Inspection of Radio Timing Solutions

Roy et al. (2015) and de Martino et al. (2020) provided radio timing solutions for J1227 that were derived for relatively short intervals (Table 2). From an initial inspection of the solutions for 12.5 years of LAT operation, we find that Solutions 1 and 2 are very similar; phase misalignment between them is only ≤ 0.03 . Solution 3 differs from the others with a phase misalignment of ~ 0.1 and so will be discernible by the 15-yr optical data. Note, however, that ignoring the second derivative from Solution 3 makes the misalignment small, at a ~ 0.05 level.

We extrapolate the solutions to the 15-year span of the optical data. Because the orbital frequency (F_B) is not expected to vary much and the timing solutions do not use high orbital frequency derivatives, the solutions seem to align well with the optical phases at various epochs in the 15 year period (Fig. 1), meaning that extrapolating the radio solutions is adequate for the orbit. However, we note that Solution 3 (red in Fig. 1) misaligns some early observations; day-night cycles seen in the light curves folded on Solutions 1 and 2 are blurred (Fig. 1 a) and the peak phase is shifted (Fig. 1 c). This implies that Solution 3 may not be accurate outside the validity window because of the second

derivative \ddot{F}_B ; simply ignoring it in the solution recovers the phase alignment.

We make more quantitative checks on the timing solutions by modeling the light curves with a sine function having time-varying frequency

$$M(t) = M_0 \sin[\omega_B(t-T_0) + \dot{\omega}_B(t-T_0)^2/2 + \ddot{\omega}_B(t-T_0)^3/6] + C, \quad (1)$$

where $M(t)$ is the magnitude, ω_B is $2\pi F_B$, and T_0 is the epoch of the ascending node. Note that we do not use the pre-transition data in the fit because of the large scatter in the data caused by dips and flares (e.g., Fig. 1 d); small inaccuracy in the phases of these data will bias the solution significantly due to the long baseline. Besides, a single sine function does not fit the data across the transition because the source was substantially brighter and the modulation amplitude appeared to be smaller in the pre-transition data than in the post-transition ones.

We fit the post-transition light curves (Fig. 1 b, e, and f) holding the frequency and its derivatives fixed at the values in Table 2, and compare χ^2 of the fits for different solutions. The χ^2 values are presented in Table 2. All the solutions are acceptable, but Solution 3 is inferior to the other ones. We also vary F_B and/or \dot{F}_B , and find that optimizing these values does not significantly improve the fits with $\chi^2/\text{dof}=216.3/235$ ($F_B = 4.02033(2) \times 10^{-5} \text{ s}^{-1}$) and $215.7/234$ ($F_B =$

Table 2. Radio timing solutions for the orbit of J1227 used in this work

Properties	Solution 1	Solution 2	Solution 3
F_B (s^{-1})	$4.02034590 \times 10^{-5}$	$4.02035224 \times 10^{-5}$	$4.02034315 \times 10^{-5}$
\dot{F}_B (s^{-2})	1.406×10^{-18}	4.04×10^{-19}	3.74×10^{-18}
\ddot{F}_B (s^{-3})	0	0	-7.77×10^{-26}
T_{ASC} (MJD)	56700.9070772	57139.0715595	56700.907021
TSTART (MJD)	56707.95	57063.530	56824.26
TSTOP (MJD)	56978.13	57233.225	57685.21
χ^2/dof	219.9/236	217.7/236	223.0/236
Refs.	Roy et al. (2015)	de Martino et al. (2020)	de Martino et al. (2020)

$4.02032(2) \times 10^{-5} s^{-1}$ and $\dot{F}_B = 2(2) \times 10^{-18} s^{-2}$); the best-fit F_B and \dot{F}_B are consistent with the radio solutions. The optical data are well fit with a model having F_B only, and including higher frequency derivatives does not provide a statistically better fit. Note that using the optimized values of F_B and/or \dot{F}_B for the LAT data does not significantly alter the results below.

3. FERMI-LAT DATA ANALYSES

We analyze *Fermi*-LAT data collected between 2008 Aug. and 2021 Feb. spanning approximately 12.5 years. The data are analyzed with the *Fermi* Science Tools (ST) v1.2.23 along with the P8R3_SOURCE_V2 instrument response.⁴ We select the Front+Back event type in the SOURCE class within an $R = 10^\circ$ region of interest (RoI), and reduce the data using the zenith angle $< 90^\circ$, DATA_QUAL>0, and LAT_CONFIG=1. A 100 MeV–300 GeV image is displayed in Figure 2, and we further analyze the data as described below.

3.1. Spectral Analysis

We first perform a binned likelihood analysis in the 100 MeV–300 GeV band to measure the source spectrum. Because our data are not very different from those used for the 4FGL catalog (`gll_psc_v21.fit`; Abdollahi et al. 2020) and the source state has not changed recently, the 4FGL values are expected to be very accurate. Nevertheless we verify the parameter values below.

We use the same spectral models as in 4FGL and fit parameters for bright sources within 3° from J1227 and amplitudes of diffuse emission⁵ (`gll_iem_v07` and `iso_P8R3_SOURCE_V2_v1`). J1227 emission is modeled with PLEXP2, $dN/dE = N_0(E/E_0)^{-\Gamma_1} e^{-aE^{\Gamma_2}}$ with E_0 and Γ_2 held fixed at 1.5 GeV and 0.67, respectively. We gradually include the next bright sources in the fit and compare the Akaike Information Criteria (Akaike 1974) fit statistics. We repeat this until the fit does not im-

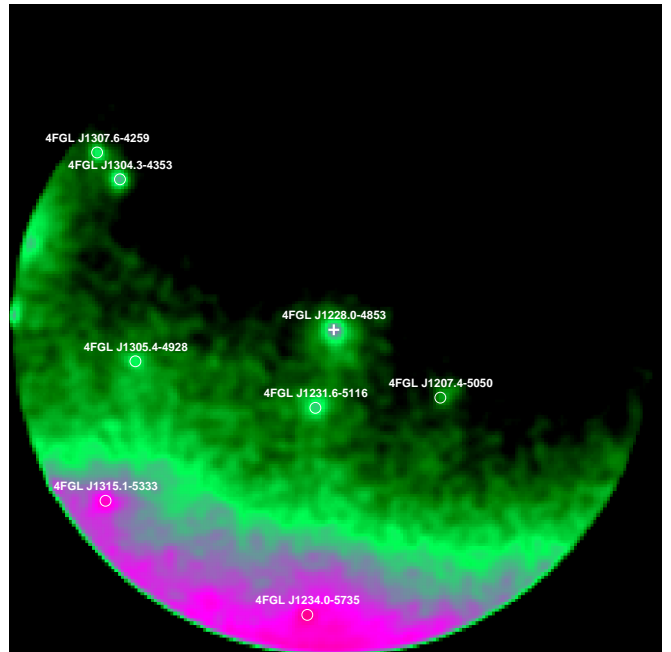


Figure 2. A *Fermi*-LAT image of a $R = 10^\circ$ field in the 100 MeV–300 GeV band. J1227 is marked with a cross at the center, and other bright sources are denoted in a circle. The image is smoothed and the scale is adjusted for better legibility.

prove significantly, which requires to fit five sources. We find that the best-fit parameters for J1227 are $N_0 = (3.7 \pm 0.6) \times 10^{-12} \text{ phs cm}^{-2} \text{ s}^{-1} \text{ MeV}^{-1}$, $\Gamma_1 = 1.6 \pm 0.1$ and $a = (7 \pm 1) \times 10^{-3}$. Since these values are consistent with those in 4FGL at the $\leq 2\sigma$ levels, we use the 4FGL model for the timing analysis. We verified that using our optimized or the 4FGL-DR2 (`gll_psc_v27.fit`) model does not significantly alter the results below.

3.2. Timing Analysis

For a timing analysis, we perform an unbinned likelihood analysis. We process the data following the standard procedure,⁶ compute a probability weight for each event using `gtsrcprob` with the 4FGL spectral

⁴ <https://fermi.gsfc.nasa.gov/ssc>

⁵ <https://fermi.gsfc.nasa.gov/ssc/data/access/lat/BackgroundModels.html>

⁶ https://fermi.gsfc.nasa.gov/ssc/data/analysis/scitools/likelihood_tutorial.html

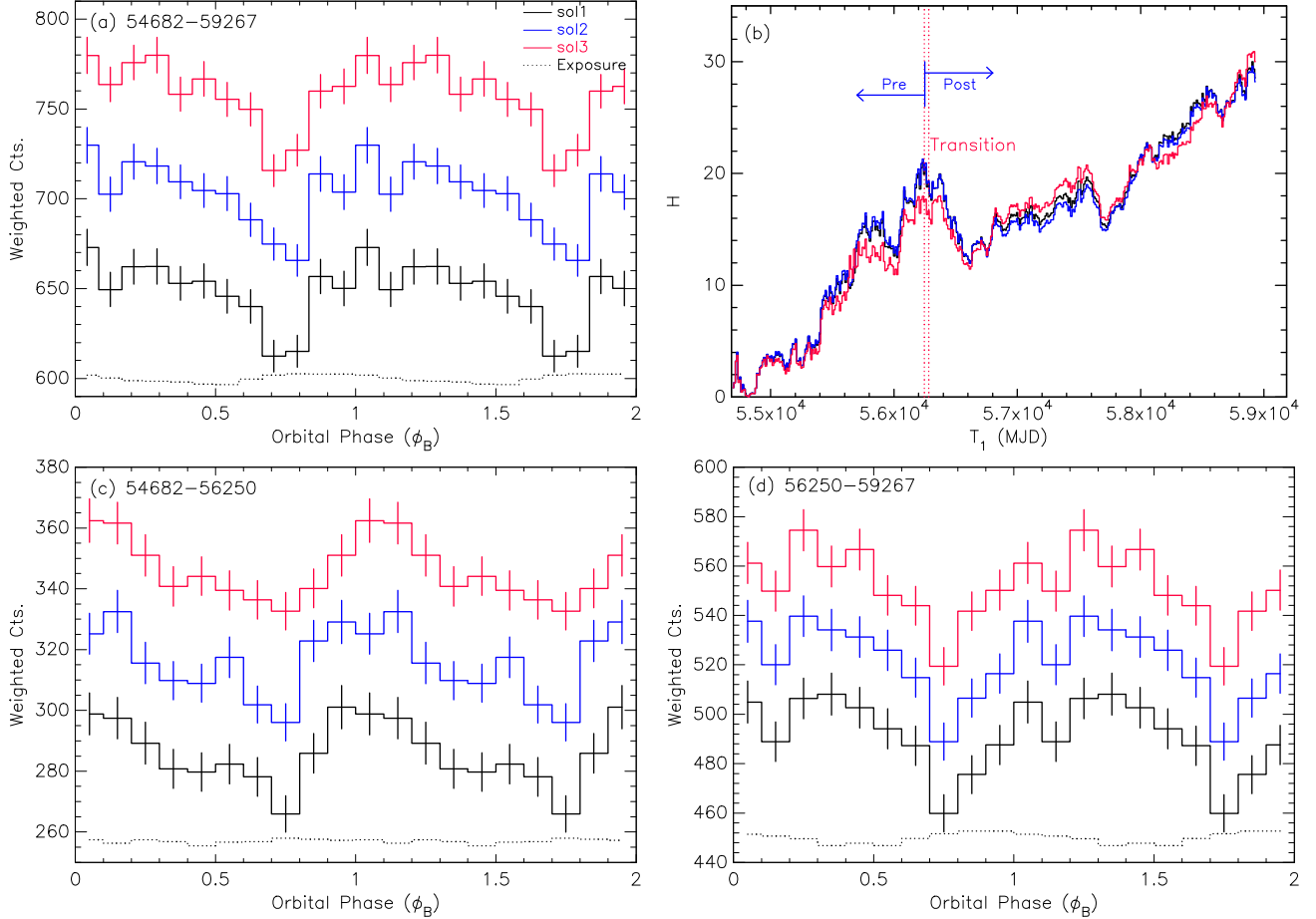


Figure 3. Exposure-corrected 60 MeV–1 GeV orbital light curves folded on the timing solutions in Table 2 (a, c, and d) and results for time-cumulative H tests (b). Black, blue, and red lines are for Solutions 1, 2, and 3, respectively, and black dotted lines show exposure variation (scaled to show in the same panels with the light curves). Time intervals for the light curves are shown in the upper left corner: full 12.5 yr (a), pre-transition (c), and post-transition (d) intervals. The blue and red light curves are displaced vertically and zero is suppressed for better legibility. $\phi_B = 0$ is the ascending node. (b) H -statistic values for the time interval T_0 – T_1 , where T_0 is the start of the LAT mission and T_1 increases from the start with a time step of 10^6 sec. Red vertical lines denote the suggested range for the state transition, and the horizontal arrows show the pre- and post-transition intervals used for light curves in (c) and (d).

models, and barycenter-correct the event arrival times with `gtbary`. Exposure is separately computed with `gtexposure`. We produce probability-weighted light curves by folding events within $R = 3^\circ$ in the low-energy band (60 MeV–1 GeV) because gamma-ray modulations have been seen better at low energies (e.g., An et al. 2018); perhaps the modulating signal drops rapidly with energy. We carry out a weighted H test (Kerr 2011) and find significant modulation of the orbital light curves for all the solutions in Table 2 with H statistics of 30, 30, and 31, for Solutions 1, 2 and 3, respectively, corresponding to $p \approx 5 \times 10^{-6}$. Changing the RoI size or energy band slightly does not alter the results significantly. The three timing solutions give similar results (here and below), and so we report only the representative ones below. Note that we also searched >1 GeV data but did not find any significant modulation. Con-

sidering this trial would make the detection significance lower by a factor of 2 (i.e., $p \approx 2 \times 10^{-6}$).

We further check to see if the low-energy modulation is induced by variation of exposure or variability of a nearby source. We fold the exposure on the same timing solutions and find that orbital variation of the exposure is only $<1\%$ (black dotted lines in Figure 3). It shows a different shape (e.g., maximum at $\phi_B=0.75$) from the light curve and thus is unlikely to induce the observed modulation of J1227. We also perform the same timing analysis for the nearby bright source 4FGL J1231.6–5116 ($\sim 2^\circ$ from J1227) and find no significant modulation ($H \approx 12$) in this source at the orbital period of J1227. Besides, the light curve of 4FGL J1231.6–5116 has a different shape (e.g., phases of minimum and maximum) from that of J1227. We also checked with other bright sources in the field (Fig. 2) and

verified that they did not exhibit significant modulation either.

The low-energy (60 MeV–1 GeV) LAT light curves have a broad bump (Fig. 3) with a minimum at $\phi_B \approx 0.75$ (IFC) as opposed to the optical (Fig. 1) and X-ray light curves (maximum at IFC; de Martino et al. 2020). This is the opposite of the result from a previous gamma-ray study (0.3–300 GeV; XW15) in which the gamma-ray maximum was suggested to be at IFC. We inspect 0.3–300 GeV data but do not find any significant modulation in that band (e.g., $H \approx 4$).

We check to see if there is energy dependence in the modulation. We split the 0.6 MeV–1 GeV band into two energy bands (60 MeV–450 MeV and 450 MeV–1 GeV) with a similar H value ($H \approx 15$ in each band). The shape of the light curve seems not to change with energy; they look almost the same as that in Figure 1 (a). However, the modulation fractions in the two sub-bands differ: $\approx 4\%$ and $\approx 10\%$ in the 60 MeV–450 MeV and 450 MeV–1 GeV bands, respectively. This implies that the modulating emission becomes weaker with energy less rapidly than the orbitally-constant pulsed emission does; the latter exponentially cuts off at high energies.

We perform a time-cumulative H test with the 60 MeV–1 GeV data by gradually increasing the time interval for the test from the start to the end of the LAT data, and find that the significance for modulation increases with time nearly monotonically except for some relatively short intervals. The result seems to suggest that the modulation is quite strong even “before” the transition (<MJD 56250) with an H value of ~ 20 . In order to confirm this we split the observation into two intervals: a pre-transition and a post-transition period (before and after MJD 56250; see blue arrows in Fig. 3 b), and compute H -statistic values for orbital modulation in each of them in the 60 MeV–1 GeV band. We find $H \approx 19$ ($p \approx 5 \times 10^{-4}$) and $H \approx 17$ ($p \approx 10^{-3}$) in the pre- and post-transition data, respectively (Fig. 3 c and d). The modulation fraction $(F_{\max} - F_{\min}) / (F_{\max} + F_{\min})$ is approximately 5% for all the pre-, post-transition, and time-integrated light curves. This possibly suggests that the gamma-ray modulation persists in both LMXB and MSP states of the tMSP J1227.

4. DISCUSSION

Because there is no long-term timing solution for the pulsar in the tMSP system J1227, we extrapolated radio timing solutions obtained over short time intervals (less than 1000 days) for the 15-year optical data and verified that the orbital solutions phase-align well the optical data. Hence, we used the extrapolated solutions for analyses of *Fermi* LAT data, and discovered

significant ($p \approx 5 \times 10^{-6}$) orbital modulation in the low-energy (60 MeV–1 GeV) gamma-ray emission of J1227. The light curves of the source have a minimum near IFC ($\phi_B = 0.75$), which is different from a previous suggestion that the gamma-ray modulation of J1227 has a maximum at that phase. We further found that the source seemed to exhibit similar modulation in the pre- and post-transition periods. The time-resolved light curves (Fig. 3 c and d), having a minimum at IFC, are similar to the time-integrated one. No significant gamma-ray modulation was detected at higher energies (>300 MeV).

XW15 claimed 3- σ gamma-ray modulation ($H \approx 11$) in the >300 MeV band assuming an orbital frequency of 4.018×10^{-5} Hz in a post-transition period, which we were not able to reproduce. Although the discrepancy may be due to differences in the datasets (“Pass 8” vs “Pass 7”), an analysis carried out with “Pass 7” data did not reproduce the >300 MeV modulation either (Johnson et al. 2015). Because the orbital frequency assumed by XW15 is not consistent with the radio solutions (Table 2) and one we found by fitting optical light curves (§ 2.2), and the detection significance is not high (would be lower considering some trial factors), we speculate that the >300 MeV modulation might be spurious.

Our investigation of the radio timing solutions suggests that higher-order derivatives (e.g., higher than the second time derivatives) of the orbital frequency seem to be small as in PSR J2039–5617 ($\Delta P_B / P_B \leq 10^{-6}$; Clark et al. 2021). Otherwise, it is very difficult to maintain the phase alignment of the optical data over the 15 yr period (e.g., Fig. 1). Our inspection of the timing solutions does not provide a definite test for them, and the current solutions may be slightly inaccurate. Small inaccuracy (e.g., ~ 10 s phase offsets for PSR J2039–5617; Clark et al. 2021) would not change our conclusions significantly since the gamma-ray modulation is detected regardless of the timing solutions we tested and so seems to be quite robust. However, phases of the gamma rays might have been mixed, which makes the light curve broader; the intrinsic gamma-ray light curve of J1227 may be somewhat narrower. The phase mixing is particularly a concern for a phase-resolved spectroscopy; a phase-resolved study awaits a better timing solution.

In time-cumulative H tests (§ 3.2) for the low-energy modulation, we find that the significance for it (i.e., H value) seems to increase more rapidly between MJDs 55400 and 56250 than at other times (Fig. 3). XW15 noted that long-term (>30 day) variability in J1227 was strong in MJD 55400–55800 and the source was brighter in MJD 55800–56250 than before. Al-

though it is unclear whether the stronger modulation and long-term variability in the time interval are related to each other, it will be intriguing to see if a physical scenario could explain a simultaneous change of orbital modulation and long-term variability in the LMXB state. Then, the large drop in cumulative H right after the transition (Fig. 3) perhaps indicates that the source might have relaxed back to a stationary state with the transition.

While gamma-ray emission in the MSP state is dominated by magnetospheric (pulsed) emission which is orbitally constant, the detection of orbitally modulating gamma rays in the MSP state of J1227 suggests that there are other emission components. The orbital modulation in the gamma-ray emission of J1227 and other pulsar binaries (e.g., Wu et al. 2012; An et al. 2017, 2018; Ng et al. 2018; An et al. 2020; Clark et al. 2021) can be explained with an IBS scenario. In the scenario (e.g., Wadiasingh et al. 2017; Kandel et al. 2019; van der Merwe et al. 2020), the alignment of optical and X-ray orbital phasing of J1227 (i.e., maximum at IFC) implies that the IBS wraps around the pulsar. If the modulating gamma rays are produced primarily via ICS of the stellar seed photons by electrons in the IBS or the pre-shock wind, the gamma-ray minimum is expected at IFC due to unfavorable viewing geometry. In the ICS-by-IBS case, however, the ICS emission can be enhanced by Doppler beaming if the IBS flow has large bulk speed and observer’s line of sight is aligned with the flow (i.e., at IFC). Then gamma-ray modulation would have a ‘maximum’ at IFC. The *Fermi*-LAT light curves of J1227, with a minimum near IFC, suggest that ICS by the pre-shock wind is the main contributor to the gamma-ray modulation or the bulk Doppler factor in the IBS flow is small.

More intriguingly, we find that J1227 seems to exhibit similar orbital modulation even in its ‘LMXB’ state (i.e., with accretion). This is very puzzling because previous models for gamma-ray emission in LMXB states seem not to predict such modulation whether the emission mechanism is ICS of disk photons by the pre-shock wind (e.g., Takata et al. 2014) or synchrotron-self-Compton at the magnetosphere-disk boundary (e.g., Papitto et al. 2014); these models may explain the stronger (i.e., compared to the MSP state) gamma-ray emission and its long-term variability in the LMXB state (e.g., >30-day scale; Johnson et al. 2015, XW15) but do not provide varying conditions in circular orbits. Because the phasings (i.e., minimum at IFC) and modulation fractions of the gamma-ray light curves in the LMXB and MSP states are similar, we speculate that ICS of the stellar photons by the pre-shock pulsar wind or IBS particles

is an important contributor to the production of modulating gamma-ray emission in the LMXB state.

Note, however, that the pre- and post-transition light curves (Figs. 3 c and d) appear qualitatively different (e.g., narrower in the LMXB state), indicating that there may be some physical differences between the two states of the source. Perhaps, the disk may play some role in the production of gamma-ray modulation. It is difficult to investigate this further because of poor quality of the light-curve measurements. Moreover, the significance of the modulation in each of the LMXB and the MSP states is yet low. Further confirmations are needed, and multiwavelength data and theoretical models can help to understand the physics behind the state change better.

It will be interesting to see if the orbital modulation of J1227 is ‘pulse-phase’ dependent as in PSR J2339–0533 (An et al. 2020). Orbital-phase-resolved spectroscopy can help to measure the ICS spectrum and model the multi-band modulation with an IBS (Takata et al. 2014; An & Romani 2017) and/or a propeller scenario (Papitto et al. 2014). These demand a more accurate timing solution that is valid through the LAT operation. While pulsar binaries are hard to time, optical data may help radio and LAT timing studies by providing a guide to orbital solutions.

ACKNOWLEDGMENTS

The *Fermi* LAT Collaboration acknowledges generous ongoing support from a number of agencies and institutes that have supported both the development and the operation of the LAT as well as scientific data analysis. These include the National Aeronautics and Space Administration and the Department of Energy in the United States, the Commissariat à l’Energie Atomique and the Centre National de la Recherche Scientifique / Institut National de Physique Nucléaire et de Physique des Particules in France, the Agenzia Spaziale Italiana and the Istituto Nazionale di Fisica Nucleare in Italy, the Ministry of Education, Culture, Sports, Science and Technology (MEXT), High Energy Accelerator Research Organization (KEK) and Japan Aerospace Exploration Agency (JAXA) in Japan, and the K. A. Wallenberg Foundation, the Swedish Research Council and the Swedish National Space Board in Sweden.

Additional support for science analysis during the operations phase is gratefully acknowledged from the Istituto Nazionale di Astrofisica in Italy and the Centre National d’Études Spatiales in France. This work

performed in part under DOE Contract DE-AC02-76SF00515.

This research was supported by Basic Science Research Program through the National Research Foundation of Korea (NRF) funded by the Ministry of Science, ICT & Future Planning (NRF-2017R1C1B2004566).

Facilities: *Swift*, *XMM-Newton*, *Fermi*

Software: *Fermi* ST (v1.2.23), HEASoft (v6.27; NASA High Energy Astrophysics Science Archive Research Center 2014), XMM-SAS (v20190531; Gabriel 2017)

REFERENCES

- Abdollahi, S., Acero, F., Ackermann, M., et al. 2020, *ApJS*, 247, 33
- Akaike, H. 1974, *IEEE Transactions on Automatic Control*, 19, 716
- Alpar, M. A., Cheng, A. F., Ruderman, M. A., & Shaham, J. 1982, *Nature*, 300, 728
- An, H., & Romani, R. W. 2017, *ApJ*, 838, 145
- An, H., Romani, R. W., Johnson, T., Kerr, M., & Clark, C. J. 2017, *ApJ*, 850, 100
- An, H., Romani, R. W., & Kerr, M. 2018, *ApJL*, 868, L8
- An, H., Romani, R. W., Kerr, M., & Fermi-LAT Collaboration. 2020, *ApJ*, 897, 52
- Archibald, A. M., Stairs, I. H., Ransom, S. M., et al. 2009, *Science*, 324, 1411
- Archibald, A. M., Bogdanov, S., Patruno, A., et al. 2015, *ApJ*, 807, 62
- Atwood, W. B., Abdo, A. A., Ackermann, M., et al. 2009, *ApJ*, 697, 1071
- Bassa, C. G., Patruno, A., Hessels, J. W. T., et al. 2014, *MNRAS*, 441, 1825
- Bhattacharya, D., & van den Heuvel, E. P. J. 1991, *PhR*, 203, 1
- Clark, C. J., Nieder, L., Voisin, G., et al. 2021, *MNRAS*, 502, 915
- de Martino, D., Papitto, A., Burgay, M., et al. 2020, *MNRAS*, 492, 5607
- de Martino, D., Belloni, T., Falanga, M., et al. 2013, *A&A*, 550, A89
- de Martino, D., Papitto, A., Belloni, T., et al. 2015, *MNRAS*, 454, 2190
- Gabriel, C. 2017, in *The X-ray Universe 2017*, 84
- Johnson, T. J., Ray, P. S., Roy, J., et al. 2015, *ApJ*, 806, 91
- Kandel, D., Romani, R. W., & An, H. 2019, *ApJ*, 879, 73
- Kerr, M. 2011, *ApJ*, 732, 38
- NASA High Energy Astrophysics Science Archive Research Center (Heasarc). 2014, HEASoft: Unified Release of FTOOLS and XANADU, ascl:1408.004
- Ng, C. W., Takata, J., Strader, J., Li, K. L., & Cheng, K. S. 2018, *ApJ*, 867, 90
- Papitto, A., de Martino, D., Belloni, T. M., et al. 2015, *MNRAS*, 449, L26
- Papitto, A., Torres, D. F., & Li, J. 2014, *MNRAS*, 438, 2105
- Papitto, A., Ferrigno, C., Bozzo, E., et al. 2013, *Nature*, 501, 517
- Roberts, M. S. E., McLaughlin, M. A., Gentile, P. A., et al. 2015, *ArXiv e-prints*, arXiv:1502.07208
- Roy, J., Ray, P. S., Bhattacharyya, B., et al. 2015, *ApJL*, 800, L12
- Takata, J., Li, K. L., Leung, G. C. K., et al. 2014, *ApJ*, 785, 131
- Tendulkar, S. P., Yang, C., An, H., et al. 2014, *ApJ*, 791, 77
- van der Merwe, C. J. T., Wadiasingh, Z., Venter, C., Harding, A. K., & Baring, M. G. 2020, *ApJ*, 904, 91
- Wadiasingh, Z., Harding, A. K., Venter, C., Böttcher, M., & Baring, M. G. 2017, *ApJ*, 839, 80
- Wu, E. M. H., Takata, J., Cheng, K. S., et al. 2012, *ApJ*, 761, 181
- Xing, Y., & Wang, Z. 2015, *ApJ*, 808, 17